This is the peer-reviewed, final accepted version for American Mineralogist, published by the Mineralogical Society of America.
The published version is subject to change. Cite as Authors (Year) Title. American Mineralogist, in press.
DOI: https://doi.org/10.2138/am-2022-8550. http://www.minsocam.org/

Revision 2:

SEM and FIB-TEM analyses on nanoparticulate arsenian pyrite: implications for Au enrichment in the Carlin-type giant Lannigou gold deposit in SW China

Jun Yan[1], Ruizhong Hu[1, 2]*, Jean S. Cline[3], Shanling Fu[1], Shirong Liu[1]

[1] *State Key Laboratory of Ore Deposit Geochemistry, Institute of Geochemistry, Chinese Academy of Sciences, Guiyang 550081, China*

[2] *College of Earth and Planetary Sciences, University of Chinese Academy of Sciences, Beijing 100049, China*

[3] *University of Nevada Las Vegas, Las Vegas, Nevada 89154, USA*

***Corresponding author.**

Email: huruizhong@vip.gyig.ac.cn (Hu R.Z.)

Always consult and cite the final, published document. See http:/www.minsocam.org or GeoscienceWorld

This is the peer-reviewed, final accepted version for American Mineralogist, published by the Mineralogical Society of America.
The published version is subject to change. Cite as Authors (Year) Title. American Mineralogist, in press.
DOI: https://doi.org/10.2138/am-2022-8550. http://www.minsocam.org/

ABSTRACT

Gold in Carlin-type gold ores is commonly hosted in the arsenian pyrite rim, but the formation of arsenian pyrite and its contribution on Au adsorption are poorly understood. Based on our previous NanoSIMS Au mapping, we conducted SEM and HR-TEM analyses to examine the Au deportment and nano-scale texture of individual auriferous arsenian pyrite grains from the giant Carlin-type Lannigou gold deposit in SW China. The results indicate that the arsenian pyrite rim is composed of numerous nanoparticulate pyrite grains (rather than a single crystal), and gold nanoparticles (Au^0) occur mainly in sub-rim with the highest Au content, which are porous and lower degree of order. We proposed that nanoparticulate arsenian pyrite attachment and aggregation is the main mechanism for the arsenian pyrite rim growth, and such mechanism is crucial for the Au efficient enrichment for this giant gold deposit.

Keywords: Nanoparticulate arsenian pyrite, nano-pore, FIB-TEM, Au efficient enrichment, Carlin-type gold deposits

Always consult and cite the final, published document. See http:/www.minsocam.org or GeoscienceWorld

This is the peer-reviewed, final accepted version for American Mineralogist, published by the Mineralogical Society of America.
The published version is subject to change. Cite as Authors (Year) Title. American Mineralogist, in press.
DOI: https://doi.org/10.2138/am-2022-8550. http://www.minsocam.org/

INTRODUCTION

The Catlin-type gold deposits (CTGDs) are mainly found in Nevada (USA) (Hofstra and Cline, 2000; Muntean and Cline, 2018) and SW China (Hu et al., 2002, 2017; Su et al., 2018). These deposits host the second largest Au resource on Earth and provide over 9% of the global gold production (Cline et al., 2005; Muntean et al., 2011; Large et al., 2011). Gold in unoxidized CTGDs is hosted exclusively in hydrothermal arsenian pyrite, which usually contains thousands of ppm Au, three orders of magnitude higher than that in typical ore fluid (<10 ppm) (Su et al., 2009; Kusebauch et al., 2019). This implies an effective mechanism to concentration Au into arsenian pyrite to form giant Au CTGDs.

Arsenian pyrite in CTGDs commonly precipitated around earlier gold-barren pyrite cores, forming core-rim texture and/or small individual arsenian pyrite grains (Su et al., 2018; Muntean et al., 2011; Cline, 2011). In addition, gold distribution in arsenian pyrite rim shows micron-scale zoning, which was interpreted to be related to ore-fluid geochemical changes during the pyrite rim growth (Barker et al., 2009; Yan et al., 2018).

Previous works concluded that Au^{+} captured in pyrite rims is strongly affected by the pyrite growth rate and mechanism (Fougerouse et al., 2019; Wu et al., 2019) and surface electronegativity (Kusebauch et al., 2019; Rickard and Luther, 2007; Deditius et al., 2014; Xian et al., 2019). Polycrystalline of arsenian pyrite were reported in previous studies, and were interpreted to have formed by Au exsolution, rapid local ore-fluid geochemical changes and/or temperature drop (Palenik et al., 2004; Deditius

Always consult and cite the final, published document. See http:/www.minsocam.org or GeoscienceWorld

This is the peer-reviewed, final accepted version for American Mineralogist, published by the Mineralogical Society of America.
The published version is subject to change. Cite as Authors (Year) Title. American Mineralogist, in press.
DOI: https://doi.org/10.2138/am-2022-8550. http://www.minsocam.org/

et al., 2008; Wu et al., 2021). However, the role of nanoparticulate pyrites and As-rich pyrite-rim formation in Au efficient enrichment in CTGDs has not been well understood.

Based on previous works on CTGDs in Nevada, we investigated the Au deportment and nano-scale texture of individual auriferous arsenian pyrites from the giant Carlin-type Lannigou gold deposit in SW China, via a combination of high-resolution transmission electron microscopy (HR-TEM) and secondary electron microscopy (SEM). We proposed that the attachment and aggregation of nanoparticulate arsenian pyrites to form As-/Au-rich rim occur during the fluctuating disequilibrium mineralization process.

GEOLOGICAL BACKGROUND

South China is composed of the Yangtze and Cathaysia blocks in the northwest and southeast, respectively, and is bounded by the North China Craton and Indochina-Simao Block to the north and southwest, respectively. The Youjiang Basin is located in the southwestern Yangtze Block (Fig. 1), and is locally known as the "Golden Triangle" due to the many Carlin-type gold deposits discovered since 1978 (Tu, 1992). The Youjiang Basin is composed of Neoarchean-Neoproterozoic metamorphic rocks and Cambrian-Triassic carbonates and shales (Hu et al., 2002; Peters et al., 2007; Su et al., 2008; Hu and Zhou, 2012; Fig. 1). Indosinian (Triassic) to Yanshanian (Jurassic-Cretaceous) granitic plutons are present only on the margin of the basin, although Triassic-Jurassic intrusions are inferred to be concealed beneath the sedimentary strata according to inherited zircon data of mafic dikes (Hu et al.,

Always consult and cite the final, published document. See http:/www.minsocam.org or GeoscienceWorld

This is the peer-reviewed, final accepted version for American Mineralogist, published by the Mineralogical Society of America.
The published version is subject to change. Cite as Authors (Year) Title. American Mineralogist, in press.
DOI: https://doi.org/10.2138/am-2022-8550. http://www.minsocam.org/

2002; Peters et al., 2007; Su et al., 2008; Hu and Zhou, 2012; Mao et al., 2013; Pi et al., 2017; Zhu et al., 2017; Fig. 1).

The Lannigou (aka. Jinfeng) gold deposit is a giant CTGD in the Youjiang Basin (Hu et al., 2002; Su et al., 2009, 2018; Fig. 1). The orebodies occur as veins and lenses in the Middle Triassic Xuman and Bianyang formations calcareous siltstone and mudstone, and are mainly controlled along steeply-dipping fault F3 (Yan et al., 2018; Zhang et al., 2003; Fig. 2). The Dachang Formation was identified at depth of Lannigou (Fig. 2A), which is widespread across the Youjiang Basin and has close genetic link to the regional low-temperature mineralization (Liu et al., 2017). Previous fluid inclusion studies on Lannigou suggested medium-low temperature (150-300°C) and low-salinity (<6 wt.% $NaCl_{eqv}$) ore fluid with no occurrence of boiling (Zhang et al., 2003; Yan et al., 2020). Major alteration styles include decarbonate, pyrite, silicic and argillic alterations (Zhang et al., 2003; Fig. 3A). As one of the largest CTGDs in China, the Lannigou deposit contains total Au reserve of over 109 tones (t) @ 3.83 g/t (Su et al., 2018). Gold at Lannigou is invisible and hosted in arsenian pyrite, which is the dominant sulfide in the auriferous quartz-sulfide veins (Su et al., 2009, 2018; Fig. 3A).

SAMPLES AND METHODS

Sample descriptions

Our samples were collected from a high-grade orebody (~7 g/t Au) at Lannigou. The auriferous pyrites are closely related to silicification with typical core-rim texture (Figs. 3A, B), as confirmed by micro-laser-Raman spectroscopy (Fig. 3C). Fractured

Always consult and cite the final, published document. See http:/www.minsocam.org or GeoscienceWorld

This is the peer-reviewed, final accepted version for American Mineralogist, published by the Mineralogical Society of America.
The published version is subject to change. Cite as Authors (Year) Title. American Mineralogist, in press.
DOI: https://doi.org/10.2138/am-2022-8550. http://www.minsocam.org/

individual auriferous pyrites were prepared for SEM analyses to examine the micro-nano structures in/between the core and rims. Polished thin sections were prepared from these samples, which were mapped via the backscattered electron (BSE), electron probe micro-analysis (EPMA) and nano-scale secondary ion mass spectrometry (NanoSIMS) techniques (Yan et al., 2018) to select the FIB-TEM analysis area. EPMA and BSE analyses were performed on a JEOL JSM7800F field emission scanning electron microscope (FE-SEM). Nano-scale elemental mapping was conducted on a CAMECA NanoSIMS 50L, with the effective ion beam depth of < 100 nm (for S-isotope analysis) and < 10 nm (for elemental mapping) (McPhail and Dowsett, 2009). Foil for TEM observation was conducted across a profile of the selected area with ~10 μm depth (Fig. 4), and thus the NanoSIMS analysis has no effect on the TEM observation. Detailed instrument conditions and procedures of EPMA and NanoSIMS mapping were as described in previous studies (Yan et al., 2018; Zhang et al., 2014, 2017).

Previous NanoSIMS mapping indicated that pyrite growth from Lannigou deposit can be divided into three stages according to the Au-As contents (Yan et al., 2018; Figs. 3D, E): Stage I As-Au-poor pyrite core is overgrown by stage II hydrothermal pyrite rim (As-rich but Au-poor), which is in turn overgrown by stage III auriferous arsenian pyrite rim. The stage III arsenian pyrite rim also can be divided into several sub-rims and the 1st sub-rim is usually characterized by highest Au concentration.

Micro-laser Raman spectroscopy

To constrain the pyrite phase of the pyrite core and rim, we performed micro-Laser Raman spectroscopic analysis using Renishaw RM 2000 and inVia Plus micro-Raman

Always consult and cite the final, published document. See http:/www.minsocam.org or GeoscienceWorld

This is the peer-reviewed, final accepted version for American Mineralogist, published by the Mineralogical Society of America.
The published version is subject to change. Cite as Authors (Year) Title. American Mineralogist, in press.
DOI: https://doi.org/10.2138/am-2022-8550. http://www.minsocam.org/

117 spectrometers, equipped with a CCD detector at the Institute of Geochemistry,
118 Chinese Academy of Sciences. The laser (532 nm) energy is 50 mW, and the
119 acquisition time for each spectrum is 30 s. Silicon (520 cm^{-1} Raman shift) was used as
120 the standard.

121 **Scanning electron microscope (SEM) imaging**

122 The analysis was performed at the State Key Laboratory of Ore Deposit
123 Geochemistry (Guiyang), Chinese Academy of Sciences. Selected pyrite grains were
124 cracked to expose the fracture surface, and the fragments were placed on the copper
125 stump by conductive tapes and carbon coated. Secondary electron (SE) images were
126 collected with a JEOL JSM7800F SEM, under the operation conditions of 10 kV
127 accelerating voltage and 10 mm working distance.

128 **In situ lift-out TEM foil by Focused Ion Beam (FIB)**

129 Based on previous NanoSIMS Au mapping (Figs. 3D-E and 5A-B; Yan et al., 2018),
130 in-situ lift-out foils for TEM analysis from same pyrites were prepared with an FEI
131 Dual Beam Focused Ion Beam/Scanning Electron Microscope (FIB/SEM) system, at
132 the Center for Lunar and Planetary Sciences, Institute of Geochemistry, Chinese
133 Academy of Sciences (Fig. 4). Polished thin sections were carbon coated and the
134 selected areas were protected by platinum coating. The foils are about 15 μm ×7 μm
135 ×70 nm in size. The areas with "curtain structures" on pyrite foils are usually caused
136 by the ion beam effect (Fig. 4D), which are avoided for the TEM analysis. The
137 vitrification of pyrite crystal may occur in the foils due to the ion beam affect, but this
138 lattice transformation can easily be observed and avoided under the bright field TEM.

Always consult and cite the final, published document. See http:/www.minsocam.org or GeoscienceWorld

This is the peer-reviewed, final accepted version for American Mineralogist, published by the Mineralogical Society of America.
The published version is subject to change. Cite as Authors (Year) Title. American Mineralogist, in press.
DOI: https://doi.org/10.2138/am-2022-8550. http://www.minsocam.org/

Detailed analysis procedures follow those of Wirth (2009) (Figs. 4, 5), and are summarized below:

(1) Positioning and Pt coating: the final thickness of the Pt layer is 2 μm, Ga^+ beam current is 50 pA for real-time observation and 300 pA for Pt coating (30 kV).

(2) Initial digging for pyrite lamella: 15 nA for rough digging and 3nA for milling (30 kV), pyrite lamella thickness is ~1 μm (Fig. 4A).

(3) Additional milling and partial cut of the pyrite lamella, 1 nA (30 kV).

(4) Final cut-off of pyrite lamella from the sample, 1 nA (30 kV).

(5) Lift out and attach to the copper grid with Pt coating, 50 pA (30 kV) (Figs. 4B-C).

(6) Final milling to <100nm thickness pyrite foil, 1 nA, 500 pA and 300 pA (30 kV) (Fig. 4D).

(7) Polishing of foil, 48 pA (5 kV) and 43 pA (2 kV).

TEM observation

Transmission electron microscopy (TEM) was conducted using an FEI field emission (FE) gun microscope Tecnai G2 F20 S-TWIN with an energy dispersive X-ray spectrometer (EDS), at the State Key Laboratory of Environmental Geochemistry, Institute of Geochemistry, Chinese Academy of Science. Point-to-point resolution is 0.24 nm, and can reach 0.19 nm in the STEM mode. The EDS detection limit is ~1 w.t.% and the analysis area for single spot is about 40 nm in diameter. The Fe-S-As peaks reflect the arsenian pyrite matrix, whilst Cu peak is mainly caused by the Cu-grid.

RESULTS

Gold deportment

Always consult and cite the final, published document. See http:/www.minsocam.org or GeoscienceWorld

This is the peer-reviewed, final accepted version for American Mineralogist, published by the Mineralogical Society of America.
The published version is subject to change. Cite as Authors (Year) Title. American Mineralogist, in press.
DOI: https://doi.org/10.2138/am-2022-8550. http://www.minsocam.org/

Typical of auriferous pyrite in CTGDs, oscillatory-zoned pyrite rim (hundreds of nm wide) was also observed in foils by bright field TEM (BFTEM) and TEM-EDS (Figs. 6A-B). Based on the positive correlation between band brightness (under BFTEM) and As-Au contents, NanoSIMS Au mapping in horizontal plane of arsenian pyrite (Yan et al., 2018; Figs. 5B, 6C) was used to indicate Au distribution in the vertical arsenian pyrite foil for TEM (Fig. 6D). Two areas in stage III pyrite rim (with different Au content) were selected to examine the quantity and occurrence of gold nanoparticles.

Under BFTEM images, abundant Au nanoparticles (diameter: 10-40 nm) were observed. Previous NanoSIMS study on the same sample has shown that the first sub-rim has the highest Au content (No. 1 rim in Fig. 6C; Yan et al., 2018), and the Au nanoparticles occur also mainly in this sub-rim (Fig. 6E). In contrast, there are only a few Au nanoparticles in the other sub-rims, with slightly lower Au content (Fig. 6F). Most of the observed gold nanoparticles is isolated from each other in pyrite rim and/or closed to nanoparticulate pyrites which have different lattice fringes from Au nanoparticles (Fig. 7A). A few of gold nanoparticles are distributed linearly within nano-fractures in arsenian pyrite (Fig. 7B).

Polycrystallinity of arsenian pyrite rim

The micro-/nano-particulate pyrites were observed by secondary electron imaging (SEI) of SEM in fractured individual auriferous pyrite (Fig. 8). Different from the crystalline core with conchoidal fractures (orange circle in Fig. 8B), nanoparticulate pyrites closed to the pyrite core show tetrahedron/irregular polyhedron shape or

Always consult and cite the final, published document. See http:/www.minsocam.org or GeoscienceWorld

This is the peer-reviewed, final accepted version for American Mineralogist, published by the Mineralogical Society of America.
The published version is subject to change. Cite as Authors (Year) Title. American Mineralogist, in press.
DOI: https://doi.org/10.2138/am-2022-8550. http://www.minsocam.org/

184 spherule aggregates (diameter 100-500 nm) (Figs. 8B-D), whilst micro-particulate
185 pyrites in the outer shell (equal to arsenian pyrite rim) show typical pyritohedron
186 shape (diameter 10-30 μm) (Fig. 8E).

187 The selected area electron diffraction (SAED) and fast Fourier transformation (FFT)
188 pattern is the primary method to evaluate pyrite crystallization. The SAED or FFT
189 patterns of monocrystalline pyrite shows dot arrays. However, patterns of
190 polycrystalline pyrite show disorganized scatters (Deditius et al., 2008). Crystallinity
191 features of the stage II and III arsenian pyrite sub-rims were examined from the inner
192 to outer of pyrite rim by BFTEM image (Figs. 5C-E, 9B-E). Different from the SAED
193 feature of pyrite core (inset in Fig. 9A), SAED patterns of pyrite rim (insets in Figs.
194 9B-E) show disorderly feature with systematic change from inner to outer of arsenian
195 pyrite rim. Highly disorder (inset in Fig. 9D) and porous features were observed in
196 early-stage III pyrite sub-rim (equal to the 1st sub-rim of arsenian pyrite in Fig.6C),
197 which contains the highest Au content (Fig. 3E; Yan et al., 2018) and amount of Au
198 nanoparticles (Fig. 6E). Nanoparticulate pyritohedron pyrites (diameter: 10 nm (Fig.
199 7A) to 200 nm (Fig. 9F)) were observed under highly-magnified BFTEM. The
200 nanoparticulate pyrites have different lattice fringes, and the matrix between them is
201 composed of smaller nanoparticulate or colloidal pyrite grains (Fig. 7A).

202 **DISCUSSION**

203 **Gold deportment in arsenian pyrite**

204 Determining the invisible gold speciation and distribution in arsenian pyrite is
205 essential in understanding the Au deposition in CTGDs (Deditius et al., 2014;

Always consult and cite the final, published document. See http:/www.minsocam.org or GeoscienceWorld

This is the peer-reviewed, final accepted version for American Mineralogist, published by the Mineralogical Society of America.
The published version is subject to change. Cite as Authors (Year) Title. American Mineralogist, in press.
DOI: https://doi.org/10.2138/am-2022-8550. http://www.minsocam.org/

206 Pokrovski et al., 2019). It is widely accepted that Au in the pyrite occurs as
207 structural-bound Au^{+} and minor submicron Au^{0} particles (Muntean et al., 2011;
208 Deditius et al., 2014; Palenik et al., 2004; Simon et al., 1999). Based on the
209 decoupling between isolated distribution of gold nanoparticles and continuous
210 variation of Au concentration revealed by the high-resolution (100 nm) NanoSIMS Au
211 mapping (Yan et al., 2018; Figs. 3E, 5B), we confirm that there is significantly more
212 structural-bound Au^{+} and/or Au^{0} atoms in the auriferous rim. Combining the absence
213 of fluid boiling in the Lannigou deposit and ore-fluid Au content of typical
214 Carlin-type gold deposits in SW China (<10 ppm) (Zhang et al., 2003; Su et al., 2009;
215 Su et al., 2009; Yan et al., 2020), we suggest that Au was mainly absorbed from
216 Au-undersaturated fluid as ionic state and/or atom clusters, rather than deposited as
217 nanoparticles from Au-supersaturated fluid.

218 Gold nanoparticles could be formed by multiple mechanisms: Previous
219 experimental studies suggested that as Au-HS complexes were adsorbed onto the
220 pyrite surface. Some S^{-2} ions in the complexes may be oxidized to S^{-1}, and form more
221 pyrite and reduce Au^{+} to Au^{0} (Kusebauch et al., 2019; Scaini et al., 1998). Exsolution
222 of Au^{0} in arsenian pyrite could be caused by Au oversaturation as solid solution state
223 in pyrite (Palenik et al., 2004; Reich et al., 2005; Deditius et al., 2014). Gold
224 atom-scale clusters could also be generated by slower pyrite crystal growth
225 (Fougerouse et al., 2016). Temperature rise or recrystallization of metastable arsenian
226 pyrite would also trigger Au nanoparticle formation, as Au^{0}-Au^{0} bonds are more

Always consult and cite the final, published document. See http:/www.minsocam.org or GeoscienceWorld

This is the peer-reviewed, final accepted version for American Mineralogist, published by the Mineralogical Society of America.
The published version is subject to change. Cite as Authors (Year) Title. American Mineralogist, in press.
DOI: https://doi.org/10.2138/am-2022-8550. http://www.minsocam.org/

energetically favorable than bonds between Au^0 and pyrite matrix (Becker et al., 2001; Mikhlin et al., 2006).

In our samples, the isolated Au nanoparticles (Fig. 7A) could be formed by accumulation of reduced Au atoms/clusters during the arsenian pyrite rim formation. In contrast, the linear distributed Au nanoparticles (Fig. 7B) were likely formed by later exsolution and accumulation, possibly led by temperature rise and/or auriferous pyrite recrystallization. Compared with the Au-poor area (Fig. 6F), there are more Au nanoparticles in 1st sub-rim of stage III, which has the highest Au content (Fig. 6E).

Growth of arsenian pyrite rim and Au adsorption

Gold-rich arsenian pyrite is commonly formed through the reaction of Au-HS complexes (e.g., $Au(HS)^0$, $Au(HS)_2^-$) in the As^-/H_2S^- bearing fluid with reactive iron in Fe-bearing carbonate minerals and occupies the vacancy of dissolved carbonate in the wall-rock (Hofstra and Cline, 2000; Muntean and Cline, 2018; Su et al., 2009; Kusebauch et al., 2019). Previous works revealed the occurrence of nanoparticulate pyrites in arsenian pyrites, which were interpreted as the phase transition of metastable arsenian pyrite, caused possibly by Au exsolution or rapid pyrite precipitation (Palenik et al., 2004; Deditius et al., 2008; Wu et al., 2021).

In our SEI and TEM analyses, the quantity and shapes of nanoparticulate pyrites in arsenian pyrite rim (Figs. 7A, 8-9) suggest that these nanoparticulate pyrites were formed from rapid disequilibrium precipitation, instead of phase transition of metastable arsenian pyrites. The different directions of nanoparticulate pyrites' lattice fringe under TEM analyses and (Fig. 7A) and multiple shapes (Fig. 8D) of

Always consult and cite the final, published document. See http:/www.minsocam.org or GeoscienceWorld

This is the peer-reviewed, final accepted version for American Mineralogist, published by the Mineralogical Society of America.
The published version is subject to change. Cite as Authors (Year) Title. American Mineralogist, in press.
DOI: https://doi.org/10.2138/am-2022-8550. http://www.minsocam.org/

249 nanoparticulate pyrites under SEM observation suggest that the pyrite rim grew by
250 attachment and aggregation, rather than by single crystal or epitaxial growing (Wu et
251 al., 2021). The highly disorder and porous feature of pyrite rims in early stage III (Fig.
252 9D) could be generated by a more fluctuating fluid conditions, and formed the first
253 sub-rim with the highest Au concentration (No. 1 sub-rim; Fig. 6C). Previous in-situ
254 NanoSIMS S-isotope and As/Au mapping supported such fluctuating fluid conditions
255 (Yan et al., 2018; Figs. 3E, 5C). The occurrence of nanoparticulate (~10 nm) and
256 colloidal (<10 nm) pyrites (Fig. 7A) suggested that the observed nano-scale zoning
257 (Figs. 6A-B) may also be caused by fluid fluctuation or diffusion-limited
258 self-organization process (Wu et al., 2019).

259 Previous studies suggested that, under such fluctuating fluid conditions, FeS_2 could
260 be supersaturated and nucleation rate of pyrite is likely much higher than growth rate,
261 and amount of pyrite nuclei were formed (Wu et al., 2021; Hu et al., 2019). Benefit
262 from the nano-scale size and the Brownian movement, these pyrite nuclei may not
263 have precipitated immediately from the fluid, but keep growing into nanoparticulate
264 pyrite (Banfield et al., 2000). Due to crystallographic parameters preference (Tan et
265 al., 2015), these nanoparticulate pyrites would preferentially attach and aggregate
266 onto the surface of pre-existing pyrite, forming the core-rim texture observed (Fig. 3),
267 as well as some auriferous arsenian pyrite clusters (Figs. 5A-B). The micro-particulate
268 pyrites (Fig. 8E) could be formed by recrystallization of nanoparticulate pyrites which
269 is similar to the transformation process from pyrite framboids to euhedral pyrite
270 (Sawlowicz, 1993).

Always consult and cite the final, published document. See http:/www.minsocam.org or GeoscienceWorld

This is the peer-reviewed, final accepted version for American Mineralogist, published by the Mineralogical Society of America.
The published version is subject to change. Cite as Authors (Year) Title. American Mineralogist, in press.
DOI: https://doi.org/10.2138/am-2022-8550. http://www.minsocam.org/

Gold adsorption could be affected by many factors. Experimental studies have demonstrated that Au can be efficiently chemisorbed by arsenian pyrite as $Au(HS)^0$ and $Au(HS)_2^-$ complexes (Fleet et al., 1997; Widler and Seward, 2002; Palenik et al., 2004; Xing et al., 2019). Previous studies showed that incorporation of arsenic and complex crystal shape could decrease the surface electronegativity of pyrite and promote Au-HS chemisorption (Deditius et al., 2008, 2014; Kusebauch et al., 2019; Xian et al., 2019). Compared with monocrystalline pyrite (diameter ~100 μm), the surface area of pyrite nanoparticles (diameter ~10 nm) is tens of thousand times higher (Langmuir, 1916) and more beneficial for Au chemisorption. The porosity of arsenic pyrite rim (Figs. 9D, F) could allow continuous chemisorption of Au by the precipitated nanoparticulate pyrites until they are solidified and isolated from the ore fluid.

IMPLICATIONS

Pyrite growth model for Au efficient enrichment

Gold nanoparticles and nanoparticulate pyrites were revealed by FIB-TEM at the stage II and III of auriferous pyrite rim in the giant Lannigou gold deposit, SW China. Based on our results, published studies of arsenian pyrite and aggregation-based crystal growth model of natural iron oxyhydroxide (Banfield et al., 2000), we proposed that auriferous pyrite growth based on attachment and aggregation is essential for Au enrichment in this giant CTGD, as explained below in detail (Fig. 10).

1. High-As and low-Au pyrite rim composed by nanoparticulate arsenian pyrites

Always consult and cite the final, published document. See http:/www.minsocam.org or GeoscienceWorld

This is the peer-reviewed, final accepted version for American Mineralogist, published by the Mineralogical Society of America.
The published version is subject to change. Cite as Authors (Year) Title. American Mineralogist, in press.
DOI: https://doi.org/10.2138/am-2022-8550. http://www.minsocam.org/

293 was formed (Figs. 10A-B) by the initial high-As and low-Au fluid pulse and pH
294 buffer effect caused by fluid-rock interaction, in which substantial H_2S is consumed to
295 produce the H^+ needed [$H_2S \rightarrow H^+ + HS^-$] for Fe-bearing carbonate dissolution
296 [$Ca(Fe)CO_3 + 2H^+ \rightarrow Ca(Fe)^{2+} + H_2O + CO_2$], which is a key factor for pyrite
297 formation in CTGDs (Cline et al., 2005; Muntean et al., 2018; Hu et al., 2002).
298 Increased HS^- would hamper Au chemisorption via $Fe(S, As)_2 + Au(HS)_2^- \rightarrow Fe(S,$
299 $As)_2 \cdot Au(HS)^0 + HS^-$ (Simon et al., 1999; Bowers, 1991).

300 2. Alternatively, with more high-As-Au ore fluid recharge and extensive
301 neutralization of acidic ore fluid, the arsenian nanoparticulate pyrites would adsorb
302 substantial amount of Au from the ore fluid, even though the fluid was
303 Au-undersaturated (Fig. 10B). Meanwhile, these auriferous arsenian nanoparticulate
304 pyrites attached on the earlier-formed low-Au pyrite would form high-Au arsenian
305 pyrite rims (Fig. 10C).

306 3. Due to temperature dropping and recrystallization of nanoparticulate pyrite,
307 native gold nanoparticles were formed by exsolution and accumulation of
308 structural-bound Au^0 grains and aggregates (Fig. 10D).

309 **Economic geology implications**

310 Pyrite is the most common sulfide in hydrothermal gold deposits, including
311 orogenic, porphyry, epithermal and volcanic-hosted massive sulfide (VHMS) types.
312 The ubiquitous zoning in pyrite from these deposits suggests that the ore fluids have
313 undergone fluctuation and disequilibrium processes (Cline et al., 2005; Deditius et al.,
314 2011, 2014; Goldfarb et al., 2005; Large et al., 2007, 2009; Reich et al., 2013; Sung et

Always consult and cite the final, published document. See http:/www.minsocam.org or GeoscienceWorld

This is the peer-reviewed, final accepted version for American Mineralogist, published by the Mineralogical Society of America.
The published version is subject to change. Cite as Authors (Year) Title. American Mineralogist, in press.
DOI: https://doi.org/10.2138/am-2022-8550. http://www.minsocam.org/

al., 2009; Thomas et al., 2011). In epithermal and VHMS deposits, colloform and nanoscale pyrites occur widely in growth or sector zoning of pyrite, with high concentrations of Au, As and Cu (Deditius et al., 2008, 2009; Barrie et al., 2009; Masslennikov et al., 2009). This suggests that nanoparticulate pyrite precipitation may be common and important for Au efficient enrichment in these hydrothermal gold deposits.

In addition, the occurrence of nano-gold may also have an impact on the Au recovery in refractory ores from these gold deposits. Currently, refractory gold ores are oxidized firstly for Au chemical leach (La Brooy et al., 1994; Eldorado Gold Corp. Ltd., 2011). A better understanding of the forming mechanism of nano-gold, including redox process of Au^{+} and temperature behavior of Au^{0}, may lead to more cost-effective methods for Au recovery.

ACKNOWLEDGEMENTS

We thank staffs from the Jinfeng Mine Ltd. for their field support, and Dr. Bing Mo for the sample preparation. This research was jointly funded by National Natural Science Foundation of China (U1812402, 41830432, 41903044) and the China Postdoctoral Science Foundation (2018M643531).

Always consult and cite the final, published document. See http:/www.minsocam.org or GeoscienceWorld

This is the peer-reviewed, final accepted version for American Mineralogist, published by the Mineralogical Society of America.
The published version is subject to change. Cite as Authors (Year) Title. American Mineralogist, in press.
DOI: https://doi.org/10.2138/am-2022-8550. http://www.minsocam.org/

REFERENCES

Banfield, J.F., Welch, S.A., Zhang, H.Z., Ebert, T.T., Penn, R.L. (2000) Aggregation-Based Crystal Growth and Microstructure Development in Natural Iron Oxyhydroxide Biomineralization Products. Science, 289, 751-754.

Barker, S., Hickey, K.A., Cline, J.S., Dipple, G.M., Kilburn, M.R., Vaughan, J.R. and Longo, A.A. (2009) Uncloaking invisible gold: use of nanoSIMS to evaluate gold, trace elements, and sulfur isotopes in pyrite from Carlin-type gold deposits. Economic Geology, 104, 897-904.

Barrie, C. D., Boyce, A. J., Boyle, A. P., Williams, P. J., Blake, K., Ogawara, T., Akai, J., Prior D. J. (2009) Growth controls in colloform pyrite. American Mineralogist, 94, 415-429.

Becker, U., Rosso, K.M. and Hochella, M.F. (2001) The proximity effect on semiconducting mineral surfaces: a new aspect of mineral surface reactivity and surface complexation theory. Geochimica et Cosmochimica Acta, 65, 2641-2649.

Bowers, T.S. (1991) The deposition of gold and other metals: pressure-induced fluid immiscibility and associated stable isotope signatures. Geochimica et Cosmochimica Acta, 55, 2417-2434.

Cline, J.S. (2001) Timing of gold and arsenic sulfide mineral deposition at the Getchell Carlin-type gold deposit, North-central Nevada. Economic Geology, 96, 75-90.

Cline, J.S., Hofstra, A.H., Muntean, J.L., Tosdal, R. M. and Hickey, K.A. (2005) Carlin-type gold deposits in Nevada: Critical geologic characteristics and viable Models, *in* Hedenquist, J.W., Thompson, J.F.H., Goldfarb, R.J., and Richards, J.P., eds., 100th Anniversary Volume. Society of Economic Geologists, Littleton, CO, 451-484.

Deditius, A.P., Utsunomiya, S., Renock, D., Ewing, R.C., Ramana, C.V., Becker, U. and Kesler, S.E. (2008) A proposed new type of arsenian pyrite: Composition, nanostructure and geological significance. Geochimica et Cosmochimica Acta, 72, 2919-2933.

Deditius, A. P., Utsunomiya, S., Ewing, R. C., Kesler S. E. (2009) Nanoscale “liquid” inclusions of As–Fe–S in arsenian pyrite. American Mineralogist, 94, 391-394.

Deditius, A. P., Utsunomiya, S., Kesler, S. E., Reich, M., Ewing R. C. (2011) Trace elements nanoparticles in pyrite. Ore Geology Reviews, 42, 32–46.

Deditius, A.P., Reich, M., Kesler, S.E., Utsunomiya, S., Chryssoulis, S.L., Walshe, J. and Ewing, R.C. (2014) The coupled geochemistry of Au and As in pyrite from hydrothermal ore deposits.

Always consult and cite the final, published document. See http:/www.minsocam.org or GeoscienceWorld

This is the peer-reviewed, final accepted version for American Mineralogist, published by the Mineralogical Society of America.
The published version is subject to change. Cite as Authors (Year) Title. American Mineralogist, in press.
DOI: https://doi.org/10.2138/am-2022-8550. http://www.minsocam.org/

362 Geochimica et Cosmochimica Acta, 140, 644-670.

363 Eldorado Gold Corp. Ltd. (2011) Technical Report for the Jinfeng Gold Mine, China.

364 Fleet, M.E. and Mumin, A.H. (1997) Gold-bearing arsenian pyrite and marcasite and
365 arsenopyrite from Carlin trend gold deposits and laboratory synthesis. American
366 Mineralogist, 82, 182-193.

367 Fougerouse, D., Reddy, S.M., Saxey, D.W., Rickard, D.A., van Riessen, A. and Micklethwaite, S.
368 (2016) Nanoscale gold clusters in arsenopyrite controlled by growth rate not concentration:
369 Evidence from atom probe microscopy. American Mineralogist, 101, 1916-1919.

370 Goldfarb, R. J., Baker, T., Dube´, B., Groves, D. I., Hart, C. J. R., Gosselin, P. (2005) Distribution,
371 character and genesis of gold deposits in metamorphic terranes. Economic Geology 100th
372 Anniversary, 100, 407-450.

373 Hofstra, A.H. and Cline, J.S. (2000) Characteristics and models for Carlin-type gold deposits.
374 Reviews in Economic Geology, 13, 163-220.

375 Hu, R.Z. and Zhou, M.F. (2012) Multiple Mesozoic mineralization events in South China-an
376 introduction to the thematic issue. Mineralium Deposita, 47, 579-588.

377 Hu, R.Z., Fu, S.L., Huang, Y., Zhou, M.F., Fu, S.H., Zhao, C.H., Wang, Y.J., Bi, X.W. and Xiao,
378 J.F. (2017) The giant South China Mesozoic low-temperature metallogenic domain-Reviews
379 and a new geodynamic model. Journal of Asian Earth Sciences, 137, 9-34.

380 Hu, R.Z., Su, W.C., Bi, X.W., Tu, G.Z. and Hofstra, A.H. (2002) Geology and geochemistry of
381 Carlin-type gold deposits in China. Mineralium Deposita, 37, 378-392.

382 Hu, S.Y., Barnes, S.J., Glenn, A.M., Pagès, A., Parr, J., MacRae, C., and Binns, R. (2019) Growth
383 history of sphalerite in a modern sea floor hydrothermal chimney revealed by electron
384 backscattered diffraction. Economic Geology and the Bulletin of the Society of Economic
385 Geologists, 114, 165–176.

386 Kusebauch, C., Gleeson, S.A. and Oelze, M. (2019) Coupled partitioning of Au and As into pyrite
387 controls formation of giant Au deposits. Science Advances, 5, eaav5891.

388 La Brooy, S.R., Linge, H.G., and Walter, G.S. (1994) Review of Au extraction from ores. Minerals
389 Engineering, 7, 1213-1241.

390 Langmuir, I. (1916) The constitution and fundamental properties of solids and liquids. Journal of
391 the American Chemical Society, 38, 2221-2295.

Always consult and cite the final, published document. See http:/www.minsocam.org or GeoscienceWorld

This is the peer-reviewed, final accepted version for American Mineralogist, published by the Mineralogical Society of America.
The published version is subject to change. Cite as Authors (Year) Title. American Mineralogist, in press.
DOI: https://doi.org/10.2138/am-2022-8550. http://www.minsocam.org/

392 Large, R. R., Maslennikov, V. V., Robert, F., Danyushevsky, L., Chang, Z. (2007) Multistage
393 Sedimentary and metamorphic origin of pyrite and gold in the giant Sukhoi Log deposit, Lena
394 gold province, Russia. Economic Geology, 102, 1233–1267.
395 Large, R. R., Danyushevsky, L., Hollit, C., Maslennikov, V. V., Meffre, S., Gilbert, S., Bull, S.,
396 Scott, R., Emsbo, P., Thomas, H., Singh, B., Foster, J. (2009) Gold and trace elements zonation
397 in pyrite using Laser Imaging Technique: implications for the timing of gold in orogenic and
398 Carlin-Style sediment-hosted deposits. Economic Geology, 104, 635–668.
399 Large, R.R., Bull, S. and Maslennikov, V. (2011) A carbonaceous sedimentary source-rock model
400 for carlin-type and orogenic gold deposits. Economic Geology, 106, 331-358.
401 Liu, J.Z., Yang, C.F. and Wang, Z.P. (2017) Geological feature of Shuiyindong Carlin-type gold
402 deposit, Guizhou, China. Geology Survey China, 4, 32-41. (In Chinese with English abstract).
403 Mao, J.W., Cheng, Y.B., Chen, M.H. and Pirajno, F. (2013) Major types and time- space
404 distribution of Mesozoic ore deposits in South China and their geodynamic settings.
405 Mineralium Deposita, 48, 267-294.
406 Masslennikov, V. V., Masslennikova, S. P., Large, R. R., Danyushevsky L. V. (2009) Study of trace
407 element zonation in vent chimneys from the Silurian Yaman-Kasy volcanic-hosted massive
408 sulfide deposit (Southern Urals, Russia) using laser ablation-inductively coupled plasma mass
409 spectrometry (LA-ICPMS). Economic Geology, 104, 1111-1141.
410 McPhail D. and Dowsett M. (2009) In: Vickerman JC, Gilmore IS, editors. Surface Analysis. The
411 Principle Techniques, Wiley.
412 Mikhlin, Y.L., Romanchenko, A.S. and Asanov, I.P. (2006) Oxidation of arsenopyrite and
413 deposition of gold on the oxidized surfaces: A scanning probe microscopy, tunneling
414 spectroscopy and XPS study. Geochimica et Cosmochimica Acta, 70, 4874-4888.
415 Muntean, J.L., Cline, J.S., Simon, A.C. and Longo, A.A. (2011) Magmatic–hydrothermal origin of
416 Nevada's Carlin-type gold deposits. Nature Geoscience, 4, 12-127.
417 Muntean, J.L. and Cline, J.S. (2018) Diversity of Carlin-style gold deposits. Reviews in Economic
418 Geology, 20, 1-6.
419 Palenik, C.S., Ustunomiya, S., Reich, M., Kesler, S.E., Wang, L. and Ewing, R.C. (2004)
420 "Invisible" gold revealed: direct imagining of gold nanoparticles in a Carlin-type deposit.
421 American Mineralogist, 89, 1359-1366.

Always consult and cite the final, published document. See http:/www.minsocam.org or GeoscienceWorld

This is the peer-reviewed, final accepted version for American Mineralogist, published by the Mineralogical Society of America.
The published version is subject to change. Cite as Authors (Year) Title. American Mineralogist, in press.
DOI: https://doi.org/10.2138/am-2022-8550. http://www.minsocam.org/

Peters, S.G., Huang, J.Z., Li, Z.P. and Jing, C.G. (2007) Sedimentary rock-hosted Au deposits of the Dian–Qian–Gui area. Ore Geology Reviews, 31, 170-204.

Pi, Q.H., Hu, R.Z., Xiong, B., Li, Q.L. and Zhong, R.C. (2017) In situ SIMS U-Pb dating of hydrothermal rutile: reliable age for the Zhesang Carlin-type gold deposit in the golden triangle region, SW China. Mineralium Deposita, 52, 1179–1190.

Pokrovski, G.S., Kokh, M.A., Proux, O., Hazemann, J.L., Bazarkina, E.F., Testemale, D., Escoda, C., Boiron, M.C., Blanchard, M., Aigouy, T., Gouy, S., Parseval, P. and Thibaut, M. (2019) The nature and partitioning of invisible gold in the pyrite-fluid system. Ore Geology Reviews, 109, 545-563.

Reich, M., Kesler, S.E., Utsunomiya, S., Palenik, C.S., Chryssoulis, S.L. and Ewing, R.C. (2005) Solubility of gold in arsenian pyrite. Geochimica et Cosmochimica Acta, 69, 2781-2796.

Reich, M., Deditius, A., Chryssoulis, S., Li, J. W., Ma, C. Q., Parada, M. A., Barra, F., Mittermayr F. (2013) Pyrite as a record of hydrothermal fluid evolution in a porphyry copper system: a SIMS/EMPA trace element study. Geochimica et Cosmochimica Acta, 104, 42-62.

Rickard, D. and Luther, G.W. (2007) Chemistry of iron sulfides. Chemical Reviews, 107, 514-562.

Sawlowicz, Z. (1993) Pyrite framboids and their development - a new conceptual mechanism. Geologische Rundschau, 82, 148-156.

Scaini, M.J., Bancroft, G.M. and Knipe, S.W. (1998) Reactions of aqueousAu^{1+} sulfide species with pyrite as function of pH and temperature. American Mineralogist, 83, 316–322.

Simon, G., Huang, H., Penner-Hahn, J.E., Kesler, S.E. and Kao, L. (1999) Oxidation state of gold and arsenic in gold-bearing arsenian pyrite. American Mineralogist, 84, 1071-1079.

Su, W.C., Dong, W.D., Zhang, X.C., Shen, N.P., Hu, R.Z., Hofstra, A.H., Cheng, L.Z., Xia, Y. and Yang, K.Y. (2018) Carlin-Type Gold Deposits in the Dian-Qian-Gui “Golden Triangle” of Southwest China. Reviews in Economic Geology, 20, 157-185.

Su, W.C., Heinrich, C.A., Pettke, T., Zhang, X.C., Hu, R.Z. and Xia, B. (2009) Sediment-hosted gold deposits in Guizhou, China: products of wall-rock sulfidation by deep crustal fluids. Economic Geology, 104, 73-93.

Su, W.C., Xia, B., Zhang, H.T., Zhang, X.C. and Hu, R.Z. (2008) Visible gold in arsenian pyrite at the Shuiyindong Carlin-type gold deposit, Guizhou, China: implications for the environment and processes of ore formation. Ore Geology Reviews, 33, 667-679.

Always consult and cite the final, published document. See http:/www.minsocam.org or GeoscienceWorld

This is the peer-reviewed, final accepted version for American Mineralogist, published by the Mineralogical Society of America.
The published version is subject to change. Cite as Authors (Year) Title. American Mineralogist, in press.
DOI: https://doi.org/10.2138/am-2022-8550. http://www.minsocam.org/

Sung, Y.-H., Brugger, J., Ciobanu, C. L., Pring, A., Skinner, W., Nugus M. (2009) Invisible gold in arsenian pyrite and arsenopyrite from a multistage Archean gold deposit: sunrise Dam Eastern Goldfields Province, Western Australia. Mineralium Deposita, 44, 765-791.

Tan, W., Wang, C.Y., He, H.P., Xing, C.M., Liang, X.L. and Dong, H. (2015) Magnetite-rutile symplectite derived from ilmenite-hematite solid solution in the Xinjie Fe-Ti oxide-bearing, mafic-ultramafic layered intrusion (SW China). American Mineralogist, 100, 2348-2351.

Thomas, H. V., Large, R. R., Bull, S. W., Masslennikov, V., Berry, R. F., Fraser, R., Froud, S., Moye R. (2011) Pyrite and pyrrhotite textures and composition in sediments, laminated quartz veins, and reefs at Bendigo gold mine, Australia: insights for ore genesis. Economic Geology, 106, 1-31.

Tu, G. (1992) Some problems on prospecting of super large gold deposits. Acta Geology Sichuan Special Issue, 12, 1-9 (in Chinese with English abstract).

Widler, T. M. and Seward, A. M. (2002) The adsorption of gold (I) hydrosulfide complexes by iron sulfide surfaces. Geochimica et Cosmochimica Acta, 66, 383-402.

Wirth, R. (2009) Focused Ion Beam (FIB) combined with SEM and TEM: Advanced analytical tools for studies of chemical composition, microstructure and crystal structure in geomaterials on a nanometre scale. Chemical Geology, 261, 217-229.

Wu, Y.F., Evans, K., Hu, S.Y., Fougerouse, D., Zhou, M.F., Fisher, L.A., Guagliardo, P. and Li, J.W. (2021) Decoupling of Au and As during rapid pyrite crystallization. Geology, 49, 827-831.

Wu, Y.F., Fougerouse, D., Evans, K., Reddy, S.M., Saxey, D.W., Guagliardo, P. and Li, J.W. (2019) Gold, arsenic, and copper zoning in pyrite: A record of fluid chemistry and growth kinetics. Geology, 47, 641-644.

Xian, H.Y., He, H.P., Zhu, J.X., Du, R.X., Wu, X., Tang, H.M., Tan, W., Liang, X.L., Zhu, R.L. and Teng, H.H. (2019) Crystal habit-directed gold deposition on pyrite: Surface chemical interpretation of the pyrite morphology indicative of gold enrichment. Geochimica et Cosmochimica Acta, 264, 191-204.

Xing, Y.L., Brugger, J., Tomkins, A. and Shvarov, Y. (2019) Arsenic evolution as a tool for understanding formation of pyritic gold ores. Geology, 47, 335-338.

Yan, J., Hu, R.Z., Liu, S., Lin, Y.T., Zhang, J.C. and Fu, S.L. (2018) NanoSIMS element mapping

Always consult and cite the final, published document. See http:/www.minsocam.org or GeoscienceWorld

This is the peer-reviewed, final accepted version for American Mineralogist, published by the Mineralogical Society of America.
The published version is subject to change. Cite as Authors (Year) Title. American Mineralogist, in press.
DOI: https://doi.org/10.2138/am-2022-8550. http://www.minsocam.org/

and sulfur isotope analysis of Au-bearing pyrite from Lannigou Carlin-type Au deposit in SW China: new insights into the origin and evolution of Au-bearing fluids. Ore Geology Reviews, 92, 29-41.

Zhang, J.C., Lin, Y.T., Yan J., Li, J.X. and Yang, W. (2017) Simultaneous determination of sulfur isotopes and trace elements in pyrite with a NanoSIMS 50L. Analytical Methods, 9, 6653-6661.

Zhang, J.C., Lin, Y.T., Yang, W., Shen, W.J., Hao, J.L., Hua, S. and Cao, M.J. (2014) Improved precision and spatial resolution of sulfur isotope analysis using NanoSIMS. Journal of Analytical Atomic Spectrometry, 29, 1934-1943.

Zhang, X.C., Spiro, B., Halls, C., Stanley, C., and Yang, K.Y. (2003) Sediment hosted disseminated gold deposits in southwest Guizhou, PRC: Their geological setting and origin in relation to mineralogical, fluid inclusion, and stable isotope characteristics. International Geology Review, 45, 407-470.

Zhu, J.J., Hu, R.Z., Richards, J.P., Bi, X.W., Stern, R., Lu, G. (2017) No genetic link between Late Cretaceous felsic dikes and Carlin-type Au deposits in the Youjiang basin, southwest China. Ore Geology Reviews, 84, 328-337.

Always consult and cite the final, published document. See http:/www.minsocam.org or GeoscienceWorld

This is the peer-reviewed, final accepted version for American Mineralogist, published by the Mineralogical Society of America.
The published version is subject to change. Cite as Authors (Year) Title. American Mineralogist, in press.
DOI: https://doi.org/10.2138/am-2022-8550. http://www.minsocam.org/

Figure captions

Fig. 1 Regional geology of the Youjiang Basin, showing the location of Lannigou Au deposit (modified after Su et al., 2018).

Fig. 2 Geological map (A) and profile (B) of the Lannigou gold deposit (after Yan et al., 2020).

Fig. 3 Core-rim texture of auriferous pyrite revealed by reflected-light, BSE and NanoSIMS: A, B: Reflected-light photos showing the auriferous pyrite coexists with quartz and clay minerals; C: micro laser-Raman spectra of pyrite core and rim, compared with standard pyrite. Standard pyrite data are from the RRUFF project database (https://rruff.info). Raman shift peaks of core and rim mimic those of standard pyrite at 341 cm^{-1} and 375 cm^{-1}; D, E: BSE and NanoSIMS Au maps of selected pyrite, showing the three pyrite growth stages (after Yan et al., 2018).

Fig. 4 Schematic diagram showing the procedure of in-situ lift-out TEM foils prepared by focused ion beam (FIB) technique: A: initial digging; B: lifting out; C: attachment to the copper grid using Pt deposition; D: final milling to <100 nm thickness and polishing. White box in D shows the "curtain" structure caused by FIB ion beam effect.

Fig. 5 Locations of the TEM foils shown in Figures 6, 7, 9: White boxes denote the TEM foil profile locations. A, B: BSE and NanoSIMS Au maps of selected pyrite shown in Figures 6-7. C: BSE image of selected pyrite shown in Figure 9. Red dots show NanoSIMS $\delta^{34}S$ values, and orange dots show EPMA arsenic content (data from Yan et al., 2018). D, E: TEM foils shown in Figure 9.

Fig. 6 Occurrence of gold nanoparticles. A, B: Arsenic oscillatory zoning revealed by

Always consult and cite the final, published document. See http:/www.minsocam.org or GeoscienceWorld

This is the peer-reviewed, final accepted version for American Mineralogist, published by the Mineralogical Society of America.
The published version is subject to change. Cite as Authors (Year) Title. American Mineralogist, in press.
DOI: https://doi.org/10.2138/am-2022-8550. http://www.minsocam.org/

523 bright field TEM image. C: NanoSIMS Au map to indicate Au content for TEM
524 observation in B. Line a-b denotes the TEM foil profile location. Numbers 1-5
525 represents the 1st to 5th Au-rich sub-rims, and the color legend is as in Figure 5. D:
526 bright field TEM image of the foil. E, F: Gold nanoparticles in bright field TEM
527 image of the Au-rich sub-rims (E) and Au-poor part (F).

528 **Fig. 7** Separated and linear distributed gold nanoparticles. A: HRTEM image of a
529 gold nanoparticle and nano-phase pyrites with different lattice fringes; B: bright field
530 TEM image showing linear distribution of gold nanoparticles; C, D: Representative
531 TEM-EDS of pyrite matrix and gold nanoparticles. Nano-Au = Au nanoparticles. Py
532 NPs= pyrite nanoparticles.

533 **Fig. 8** Nano-phase pyrites from fractured auriferous pyrite: A: SEI image of the
534 cracked pyrite grain. The majority of this grain is gold-barren core with bits of stage II
535 pyrite rim; B, C: magnified SEI image of selected area; D: Nano-pores and
536 nanoparticulate pyrites (distinct from broken pyrite fragments in Figure 8B) with
537 irregular or spherical shape; E: microparticulate pyrites in stripy stage II and III pyrite
538 rim.

539 **Fig. 9** Nano-phase pyrites revealed by FIB-TEM. A-E: bright field TEM images
540 showing the core and inner to outer rim, and their respective SAED patterns are
541 shown in the insets. White-dashed circles in A-E shown the SAED locations; F: bright
542 field TEM image of nanoparticulate arsenian pyrites (50-100 nm diameter)
543 (white-dashed polygon). Nano-Py = nanoparticulate pyrite.

544 **Fig. 10** Schematic diagram for the auriferous arsenian pyrite rims growth and Au

Always consult and cite the final, published document. See http:/www.minsocam.org or GeoscienceWorld

This is the peer-reviewed, final accepted version for American Mineralogist, published by the Mineralogical Society of America.
The published version is subject to change. Cite as Authors (Year) Title. American Mineralogist, in press.
DOI: https://doi.org/10.2138/am-2022-8550. http://www.minsocam.org/

545 adsorption. Black dots and spots denote the dissolved Au (Au^{+} and Au^{0}) and Au

546 nanoparticles, respectively.

547

Always consult and cite the final, published document. See http:/www.minsocam.org or GeoscienceWorld

This is the peer-reviewed, final accepted version for American Mineralogist, published by the Mineralogical Society of America.
The published version is subject to change. Cite as Authors (Year) Title. American Mineralogist, in press.
DOI: https://doi.org/10.2138/am-2022-8550. http://www.minsocam.org/

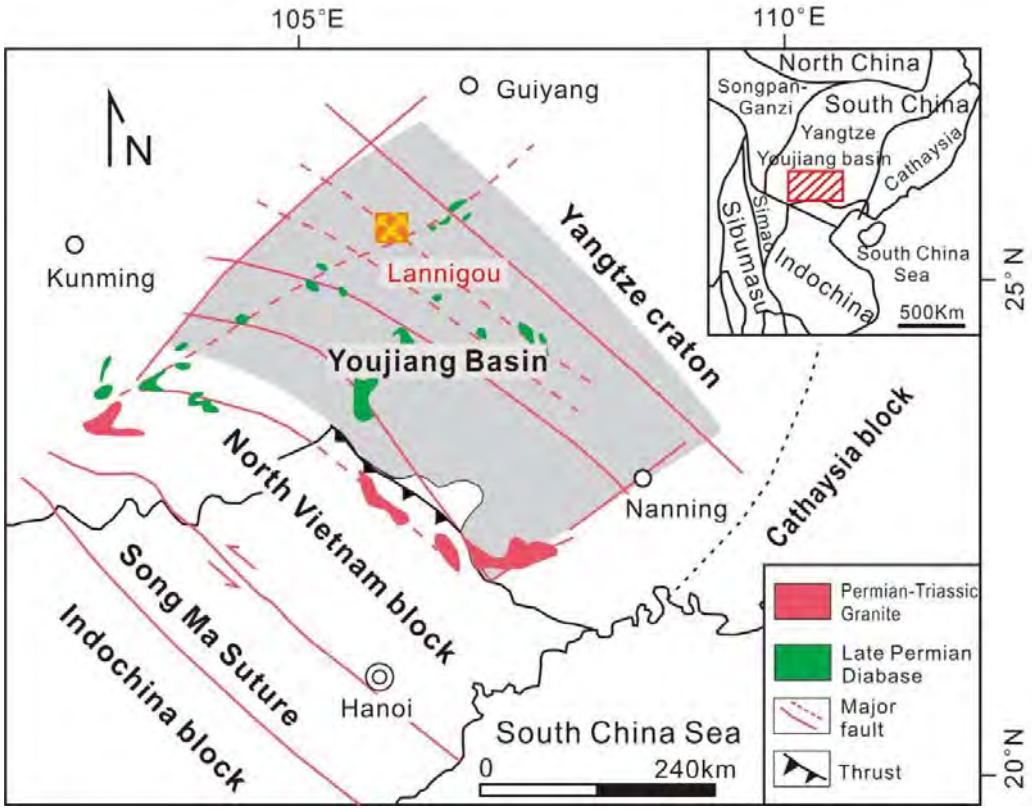

Fig. 1

Always consult and cite the final, published document. See http:/www.minsocam.org or GeoscienceWorld

This is the peer-reviewed, final accepted version for American Mineralogist, published by the Mineralogical Society of America.
The published version is subject to change. Cite as Authors (Year) Title. American Mineralogist, in press.
DOI: https://doi.org/10.2138/am-2022-8550. http://www.minsocam.org/

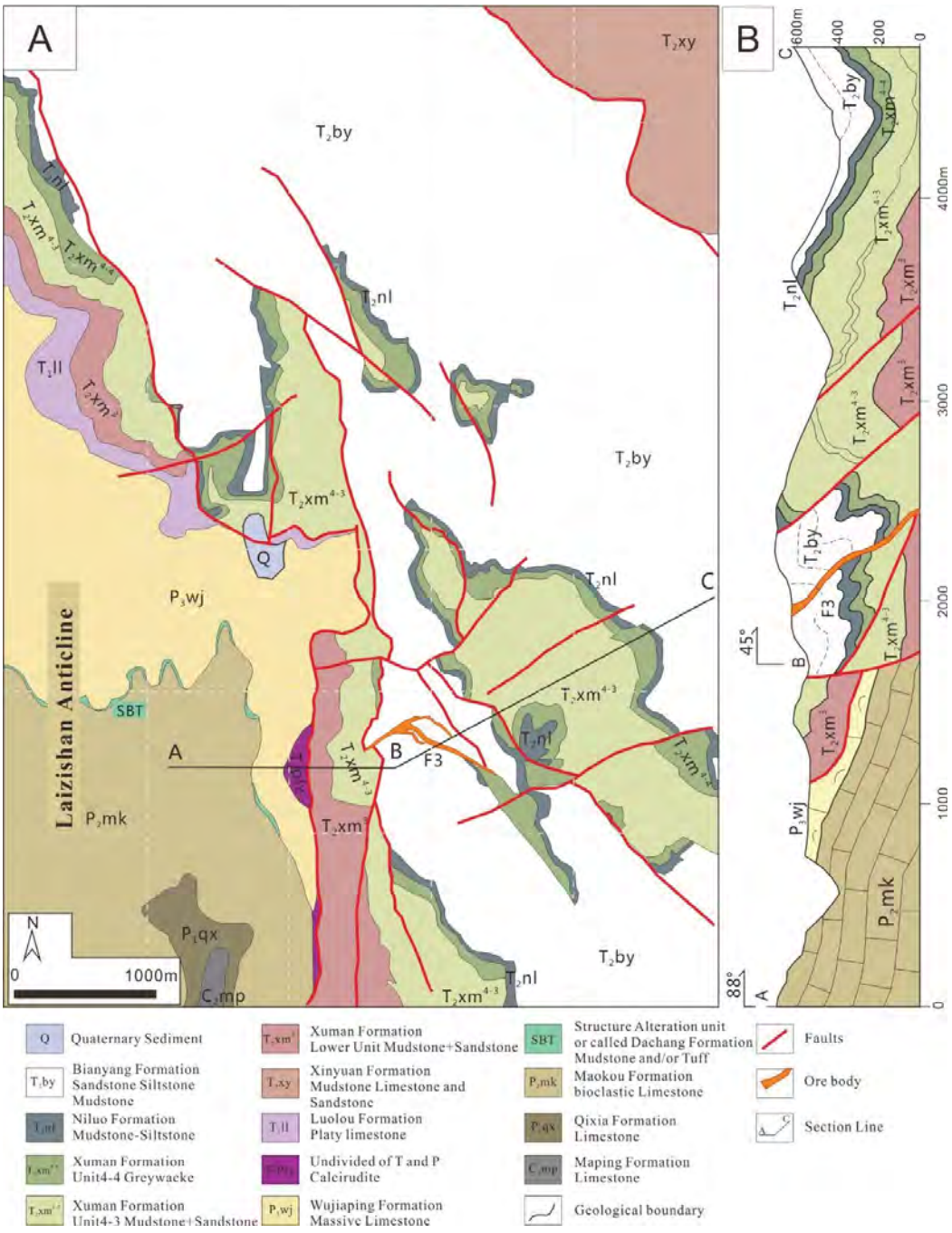

Fig. 2

Always consult and cite the final, published document. See http:/www.minsocam.org or GeoscienceWorld

This is the peer-reviewed, final accepted version for American Mineralogist, published by the Mineralogical Society of America.
The published version is subject to change. Cite as Authors (Year) Title. American Mineralogist, in press.
DOI: https://doi.org/10.2138/am-2022-8550. http://www.minsocam.org/

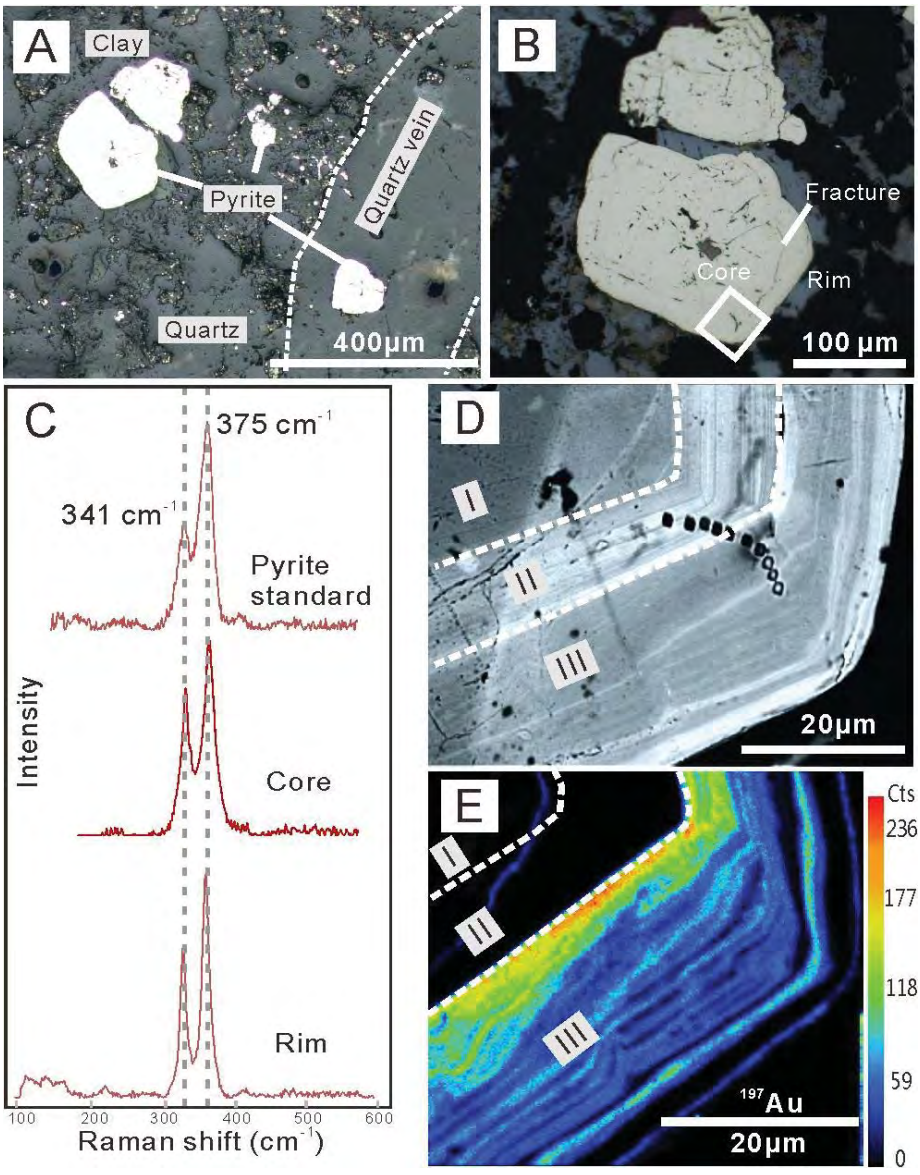

Fig. 3

Always consult and cite the final, published document. See http:/www.minsocam.org or GeoscienceWorld

This is the peer-reviewed, final accepted version for American Mineralogist, published by the Mineralogical Society of America.
The published version is subject to change. Cite as Authors (Year) Title. American Mineralogist, in press.
DOI: https://doi.org/10.2138/am-2022-8550. http://www.minsocam.org/

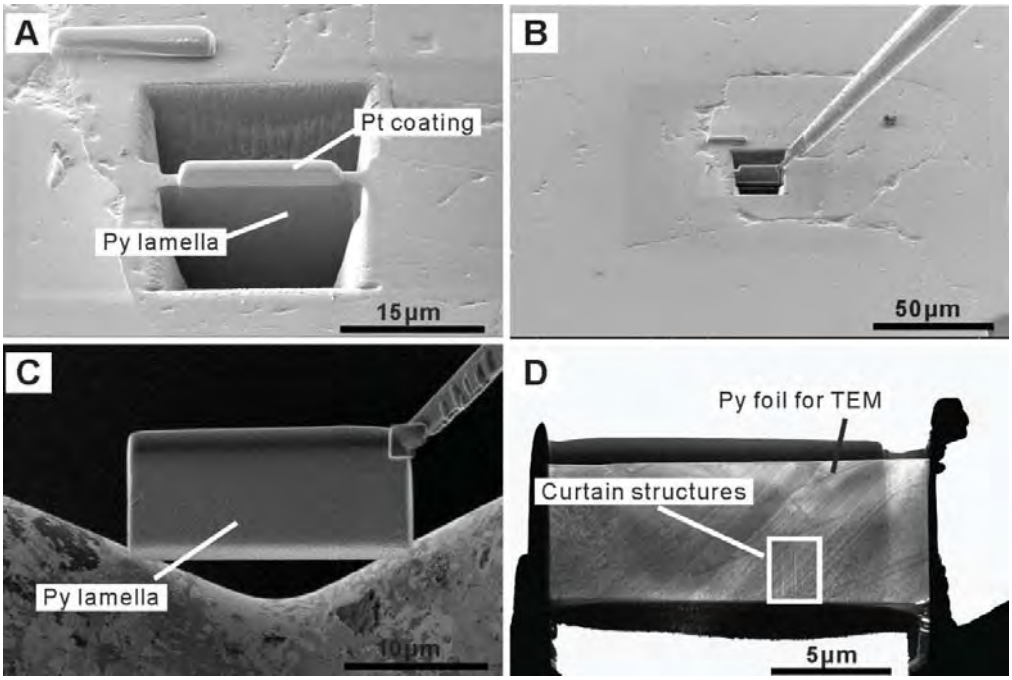

Fig. 4

Always consult and cite the final, published document. See http:/www.minsocam.org or GeoscienceWorld

This is the peer-reviewed, final accepted version for American Mineralogist, published by the Mineralogical Society of America.
The published version is subject to change. Cite as Authors (Year) Title. American Mineralogist, in press.
DOI: https://doi.org/10.2138/am-2022-8550. http://www.minsocam.org/

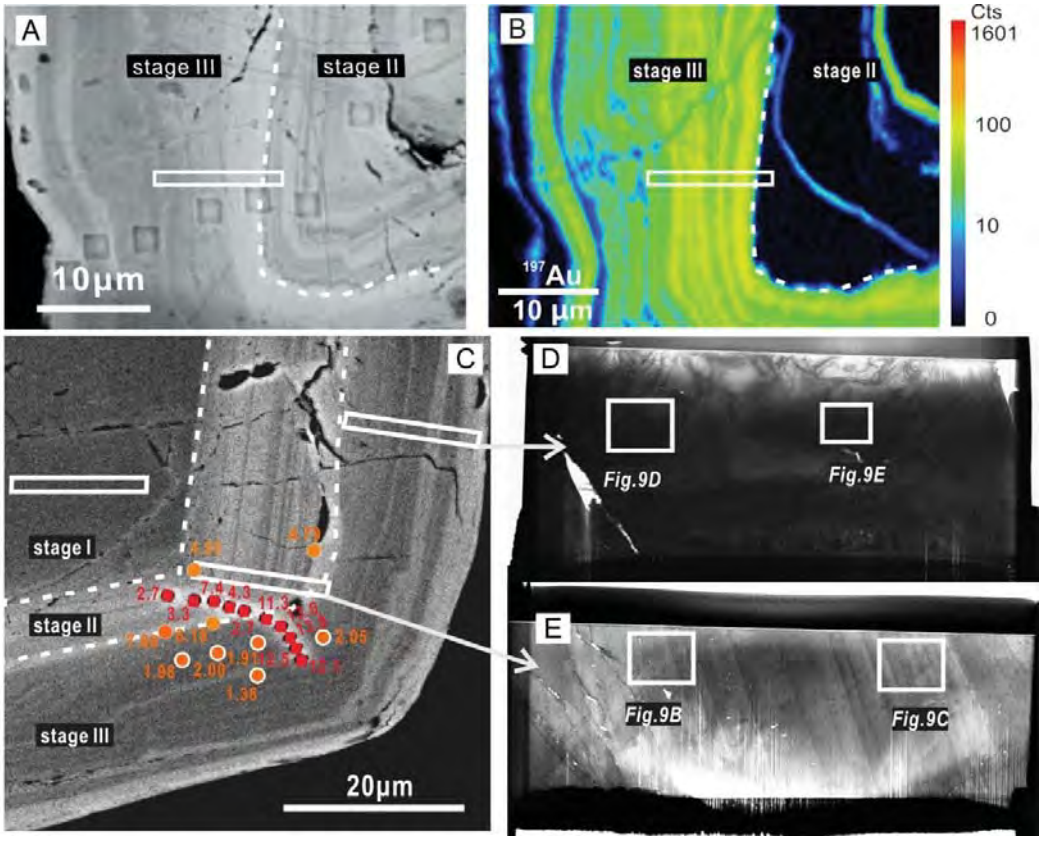

Fig. 5

Always consult and cite the final, published document. See http:/www.minsocam.org or GeoscienceWorld

This is the peer-reviewed, final accepted version for American Mineralogist, published by the Mineralogical Society of America.
The published version is subject to change. Cite as Authors (Year) Title. American Mineralogist, in press.
DOI: https://doi.org/10.2138/am-2022-8550. http://www.minsocam.org/

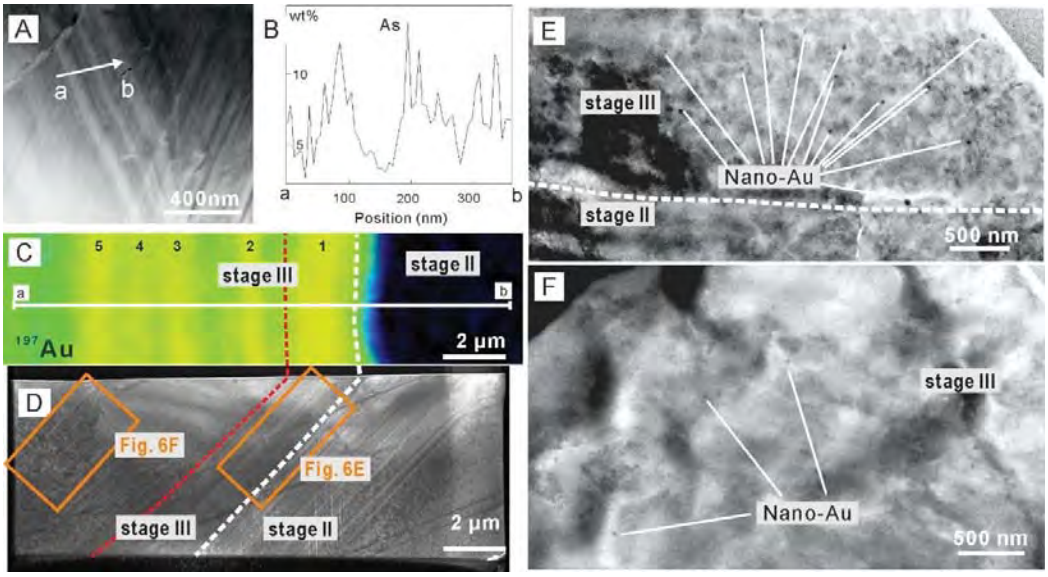

Fig. 6

Always consult and cite the final, published document. See http:/www.minsocam.org or GeoscienceWorld

This is the peer-reviewed, final accepted version for American Mineralogist, published by the Mineralogical Society of America.
The published version is subject to change. Cite as Authors (Year) Title. American Mineralogist, in press.
DOI: https://doi.org/10.2138/am-2022-8550. http://www.minsocam.org/

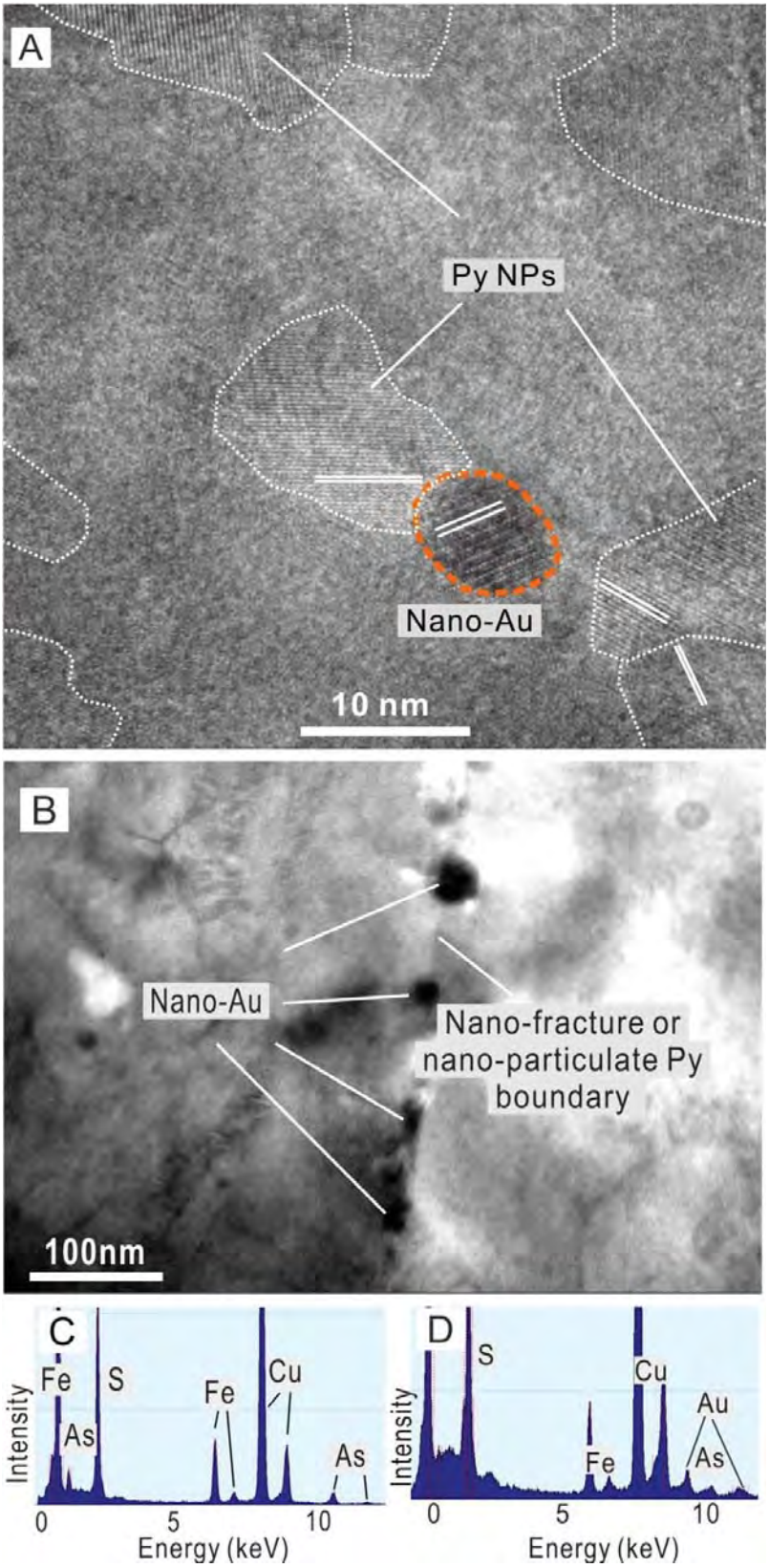

Fig. 7

Always consult and cite the final, published document. See http:/www.minsocam.org or GeoscienceWorld

This is the peer-reviewed, final accepted version for American Mineralogist, published by the Mineralogical Society of America.
The published version is subject to change. Cite as Authors (Year) Title. American Mineralogist, in press.
DOI: https://doi.org/10.2138/am-2022-8550. http://www.minsocam.org/

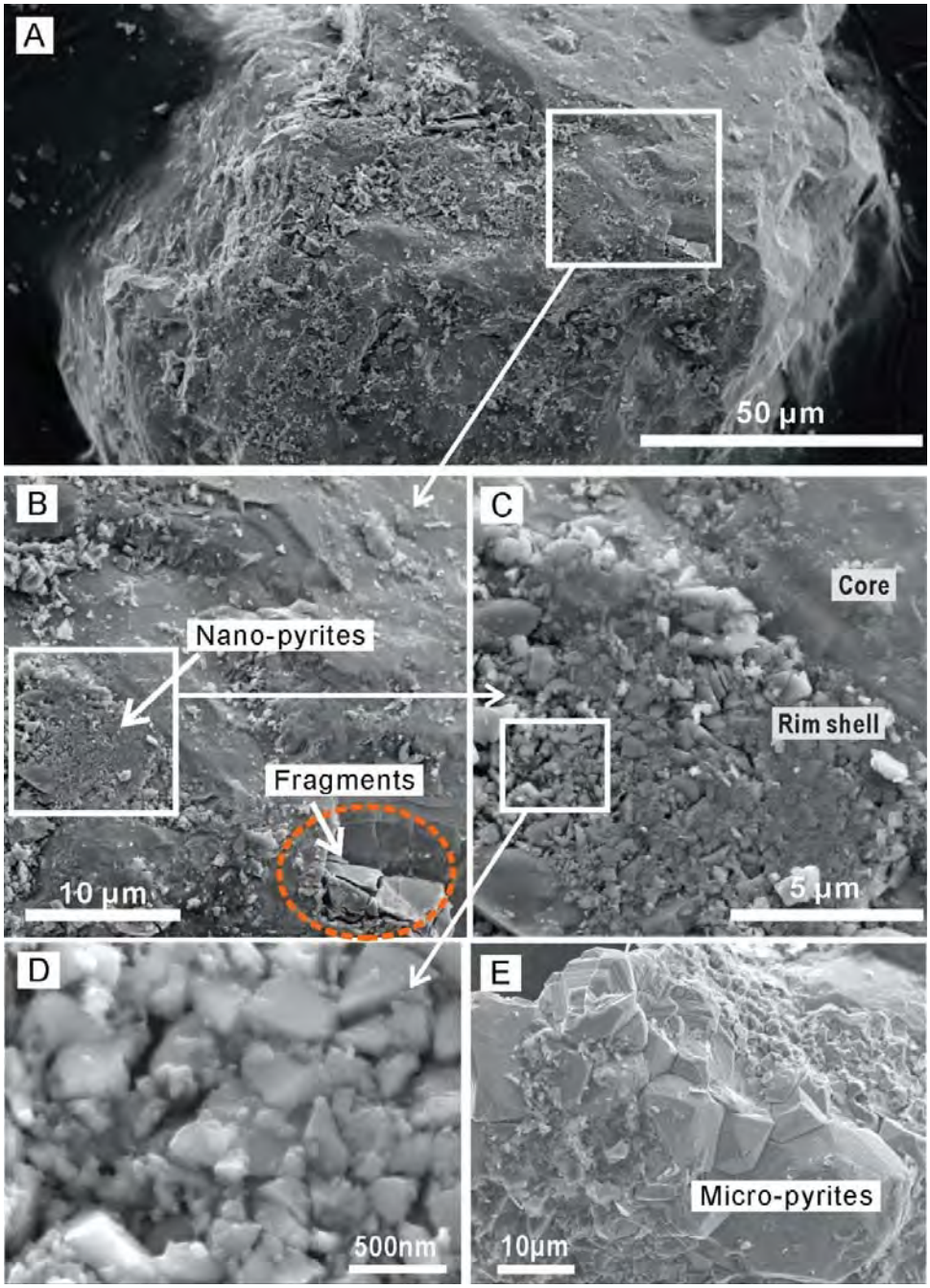

Fig. 8

Always consult and cite the final, published document. See http:/www.minsocam.org or GeoscienceWorld

This is the peer-reviewed, final accepted version for American Mineralogist, published by the Mineralogical Society of America.
The published version is subject to change. Cite as Authors (Year) Title. American Mineralogist, in press.
DOI: https://doi.org/10.2138/am-2022-8550. http://www.minsocam.org/

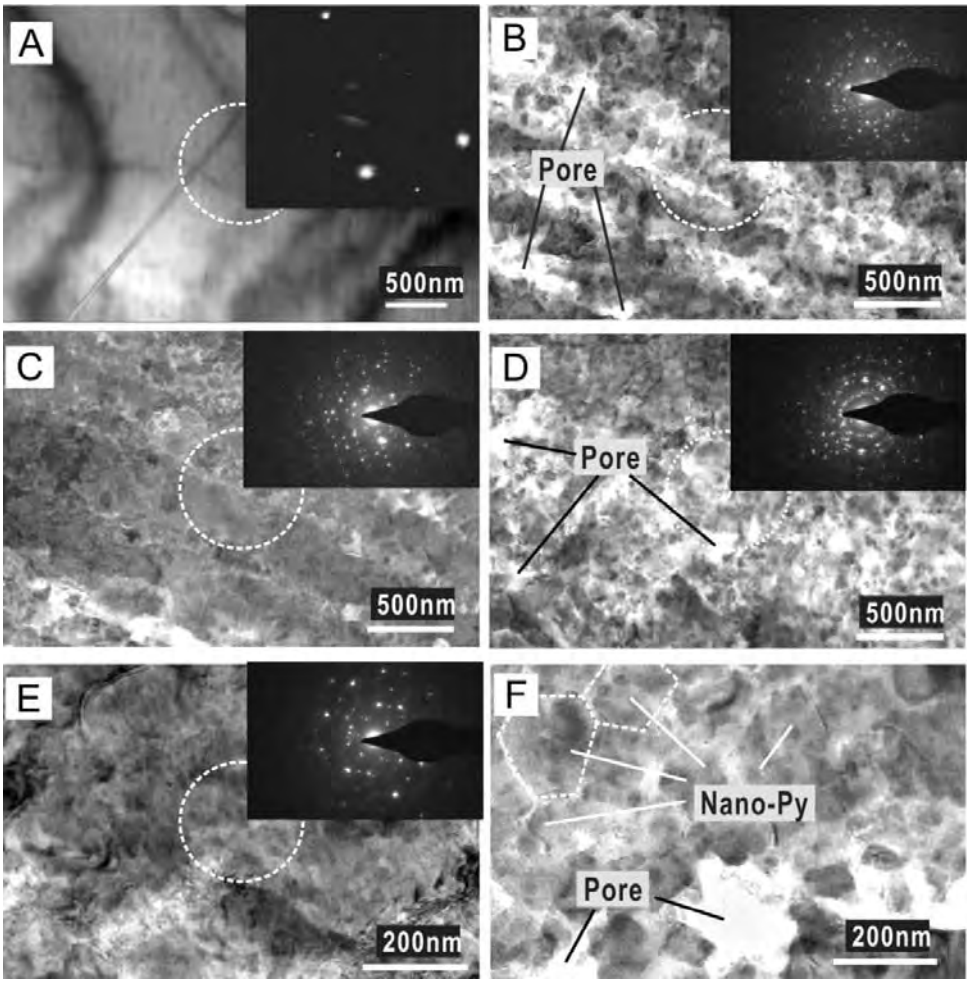

Fig. 9

Always consult and cite the final, published document. See http:/www.minsocam.org or GeoscienceWorld

This is the peer-reviewed, final accepted version for American Mineralogist, published by the Mineralogical Society of America.
The published version is subject to change. Cite as Authors (Year) Title. American Mineralogist, in press.
DOI: https://doi.org/10.2138/am-2022-8550. http://www.minsocam.org/

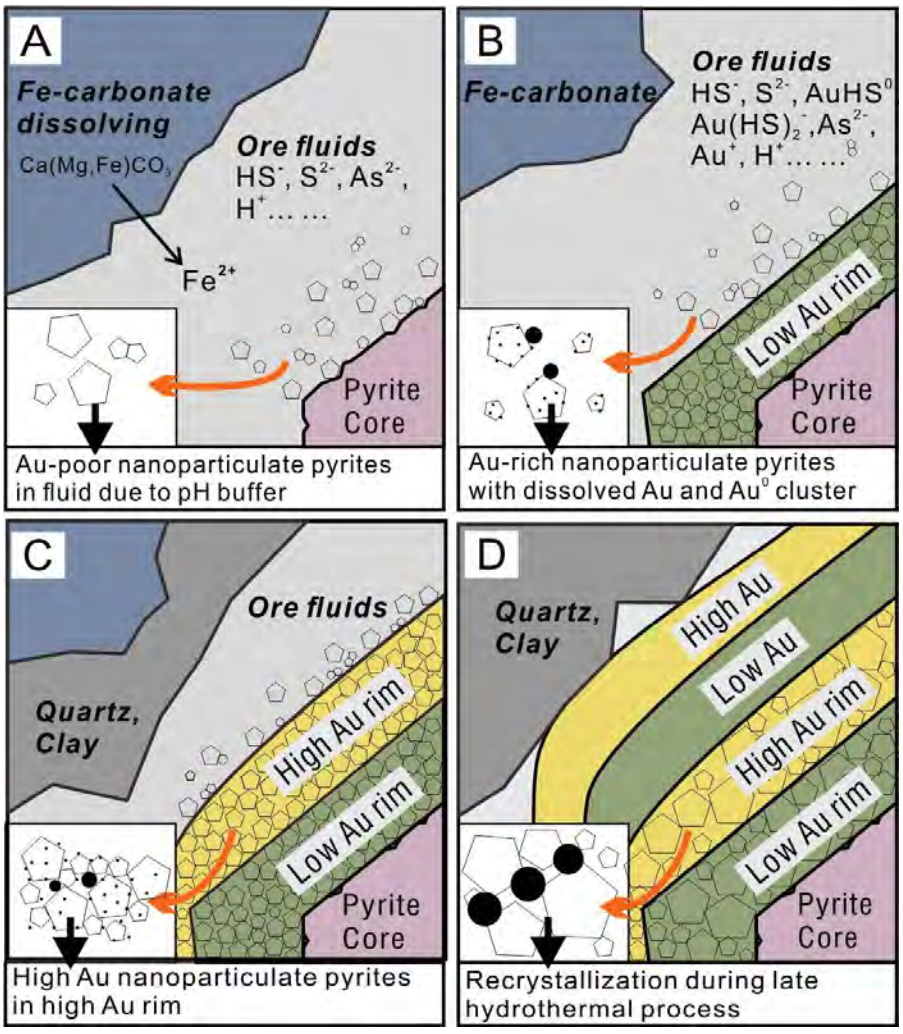

Fig. 10

Always consult and cite the final, published document. See http:/www.minsocam.org or GeoscienceWorld